

NiCo₂O₄/P,N-Doped Carbon with Engineered Interface to Improve the Rechargeability of Zn-Air Batteries at High Energy Demands

Alexander Suárez-Barajas,^[a] Minerva Guerra-Balcázar,^[b] Carlos M. Ramos-Castillo,^[a] Lorena Álvarez-Contreras,*^[c] and Noé Arjona*^[a]

The search for cost-effective, high-performance bifunctional catalysts for Zn-air batteries (ZABs) requires extensive research into precious-metal-free materials. This study provides insight into the synergy between nickel cobaltite and P,N-doped carbon modified through interface engineering by inducing oxygen vacancies in the spinel and non-metallic heteroatoms in the carbon material. NiCo₂O₄ with various oxygen vacancy levels was synthesized via an ethylene glycol-assisted solvothermal route. This resulted in significant changes in the structural and morphological properties, such as reduced crystallite size, lattice distortion, and increased oxygen vacancies, as observed from the physicochemical results. This was further verified by X-ray photoelectron spectroscopy (XPS) and high-resolution transmission electron microscopy (HR-TEM), which showed a homo-

geneous dispersion of nickel cobaltite nanorods on the carbonaceous matrix, along with an increased concentration of pyridinic nitrogen and the formation of P–N and P–C bonds, both of which enhance electrocatalytic activity. NiCo₂O₄/DI/P,N–C exhibited superior discharge polarization behavior, achieving power and current densities of 124.4 mW cm⁻² and 215.8 mA cm⁻². Stability tests revealed that the catalyst had excellent performance, lasting up to 100 h, while Pt-IrO₂/C lasted only up to 21 h. These results demonstrate the great potential of tailoring surface defects and heteroatom doping via interface engineering, resulting in high-performance precious-metal-free electrocatalysts for long-lasting and high-efficiency ZABs.

Introduction

To satisfy the growing requirements of electrochemical energy storage systems with high energy densities, it is essential to advance in commercial and next-generation renewable energy technologies.^[1] This necessity has driven extensive research and the worldwide adoption of renewable energy systems in the development of rechargeable batteries. The rising demand for electric vehicles (EVs) and Internet of Things (IoT) sensors has drawn attention to the critical need for efficient and high-performance energy storage solutions.^[2] Historically, LiBs have dominated the rechargeable landscape owing to their high specific energy of 250 Wh kg⁻¹_{cell} and are projected to continue their dominance in the following years.^[3] However, materials science

and electrochemical engineering research is shifting rapidly to other alternatives because of the high cost (250 US \$ kWh⁻¹), toxicity, and safety issues associated with LiBs.^[4]

One prospective alternative is rechargeable metal-air batteries, which can efficiently utilize the electrochemical reduction of atmospheric oxygen and provide affordability, long life, and high energy density.^[5] Zinc-air batteries are representative of this class of devices and have several advantages such as low price (\$20 per Zn kg), high energy density (1218 Wh kg⁻¹), and volumetric energy density (6136 Wh L⁻¹).^[6] These attributes have positioned ZABs as viable and realistic options, as evidenced by their commercialization by several companies, including EOS Energy Storage, Fluidic Energy, and ZincNyx.^[2b,7] Notwithstanding the potential of ZABs, research and development still needs to be undertaken to address problems in zinc electrodes, electrolytes, and air electrodes.^[8] The present study focuses on the limitations of the air electrode, especially the non-availability of active and durable bifunctional electrocatalysts.^[6a] This has motivated researchers around the world to investigate different strategies for finding suitable candidates other than noble metals, such as Pt and IrO₂, which are largely electroactive for oxygen reduction reactions (ORR) during discharge and oxygen evolution reactions (OER) during charging. Resource limitations coupled with the high cost of these noble metals make large-scale applications a challenge. This has created the emerging need for efficient bifunctional materials that accomplish comparable or better catalytic performance while remaining economically viable.^[9]

[a] A. Suárez-Barajas, C. M. Ramos-Castillo, N. Arjona

Centro de Investigación y Desarrollo Tecnológico en Electroquímica, Parque Tecnológico Querétaro S/N, SanFandila, Pedro Escobedo, Querétaro C.P. 76703, México
E-mail: wvelazquez@cideteq.mx

[b] M. Guerra-Balcázar

Facultad de Ingeniería, División de Investigación y Posgrado, Universidad Autónoma de Querétaro, Querétaro, C. P. 76010, México

[c] L. Álvarez-Contreras

Centro de Investigación en Materiales Avanzados, Complejo Industrial Chihuahua, Chihuahua, C. P. 31136, México
E-mail: lorena.alvarez@cimav.edu.mx

 Supporting information for this article is available on the WWW under <https://doi.org/10.1002/batt.202400702>

Recent attempts have increasingly focused on utilizing abundant material sources in the Earth's crust, such as transition metals,^[10] metal oxides, bimetallic oxides (like the nickel cobaltite),^[11] metal-free carbon,^[12] carbon-supported transition metal compounds,^[13] and heteroatom-doped carbons (N, S, B, F, and P).^[14] Although significant progress has been made in developing catalytically active structures from these materials, substantial potential for further enhancement still prevails. In this context, studying their efficient combinations seems quite logical and very promising. For instance, with the help of heteroatom co-doping-supported bimetallic oxides such as NiCo₂O₄/P,N-C. For this purpose, a novel approach was designed involving the interfacial coupling of defect-engineered NiCo₂O₄ with polyaniline-derived doped carbon catalysts (phosphorus- and nitrogen-doped carbon supports). NiCo₂O₄ was synthesized with variable oxygen vacancies that affected its structural and morphological properties by utilizing an ethylene glycol-assisted solvothermal method.

The integration of phosphorus and nitrogen-doped carbon supports significantly reduced the overpotential and Tafel slope of the NiCo₂O₄/P,N-C composites. Electrochemical studies revealed improved discharge polarizations with a peak power density as high as 124.4 mW cm⁻² and a maximum current density of 215.8 mA cm⁻², far surpassing benchmark materials. Long-term stability tests were conducted using this catalyst, which proved to have sustained performance for as long as 100 h. Computational studies on the modification of the electronic structure using DFT+U calculations have elucidated experimental observations. These findings demonstrate the potential of such catalysts for high-efficiency long-lasting Zn-air batteries, marking a substantial advancement in the field.

Results and Discussion

Physicochemical Characterization of NiCo₂O₄

Efficient hydrothermal methods were employed to synthesize bimetallic hydroxides with various percentages of EG used as the solvent in the synthesis process: 0% EG was named NiCo₂(OH)DI, 66% EG as NiCo₂(OH)EG₆₆, and 100% EG as NiCo₂(OH)EG. To determine the optimal temperature for the transition between bimetallic hydroxides and bimetallic spinel, thermal gravimetric analysis (TGA) was performed from room temperature to 600 °C (Figure 1a). Heat absorption began at approximately 240 °C, with a local minimum in the thermocalorimetric reduction from 325 °C to 350 °C for all three synthesized materials. The maximum differential temperature was reached at 375 °C, and a mass loss of approximately 30% was observed during the transition from the hydroxide phase to the bimetallic oxide spinel form. NiCo₂O₄DI, NiCo₂O₄EG₆₆, and NiCo₂O₄EG spinels were synthesized at 350 °C for 3 h to ensure the lowest temperature necessary for complete phase transformation.

The phase structures of the synthesized materials were characterized by XRD (Figure 1b), and six prominent diffraction

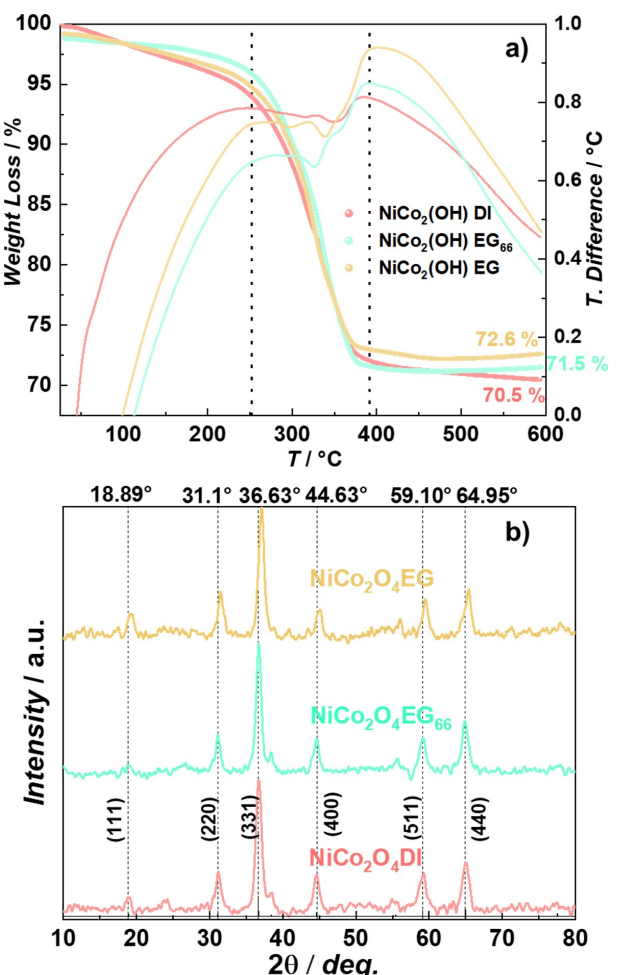


Figure 1. (a) thermal gravimetric analysis (TGA) and heat adsorption curves of NiCo₂(OH)DI, NiCo₂(OH)EG₆₆, and NiCo₂(OH)EG. (b) XRD patterns of NiCo₂O₄DI, NiCo₂O₄EG₆₆, and NiCo₂O₄EG

peaks were observed at 18.9°, 31.1°, 36.63°, 44.63°, 59.10°, and 64.95°, corresponding to the (111), (220), (311), (400), (511), and (440) crystal planes of the NiCo₂O₄ structure (JCPDS card No.00-020-0781, $a=8.114\text{ \AA}$, space group Fd-3 m (227)).^[15] A significant shift towards higher angles (2θ) was observed for each of the crystal planes in the NiCo₂O₄EG material, indicating a reduction in the interplanar distances and distortion of the crystal lattice. This shift can be attributed to a decrease in crystallite size, likely caused by defects such as oxygen vacancies introduced by the reducing agent EG during synthesis.^[16] To elucidate potential changes in morphology and microstructure, analyses were conducted using scanning electron microscopy (SEM) and high-resolution transmission electron microscopy (HR-TEM), as shown in Figure 2.

As illustrated in Figures 2a–c, NiCo₂O₄DI exhibits a characteristic structure of needle-like nanorods,^[17] with an estimated average width of approximately $11.48 \pm 3.19\text{ nm}$. These structures became increasingly aggregated as the EG content in the synthesis increased, eventually forming hemispherical shapes, as observed in Figures 2i–k for NiCo₂O₄EG. The average particle size of these aggregated nanoparticles was $10.63 \pm$

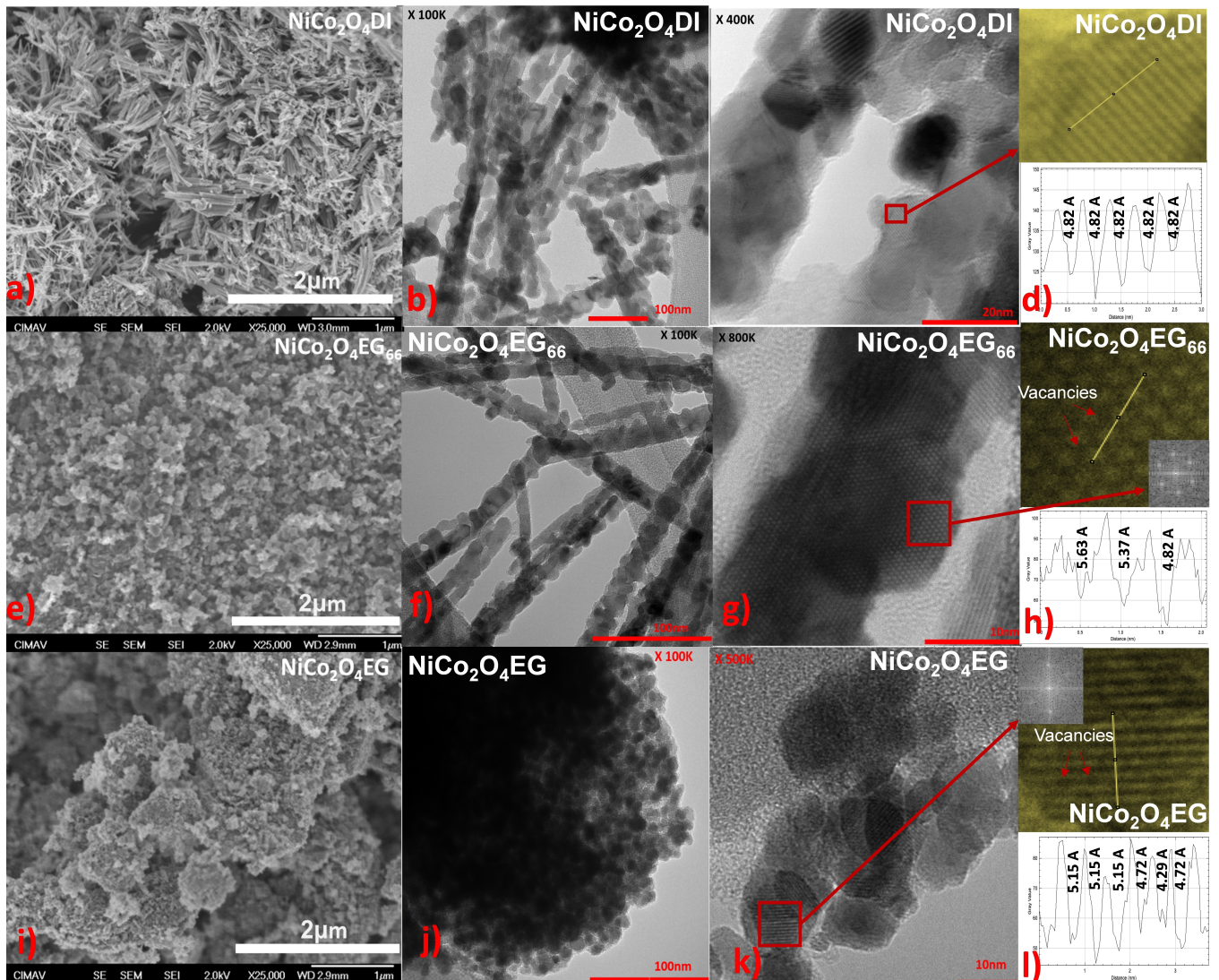


Figure 2. SEM images of a) $\text{NiCo}_2\text{O}_4\text{DI}$, e) $\text{NiCo}_2\text{O}_4\text{EG}_{66}$, and i) $\text{NiCo}_2\text{O}_4\text{EG}$. TEM images of $\text{NiCo}_2\text{O}_4\text{DI}$ (c-d), $\text{NiCo}_2\text{O}_4\text{EG}_{66}$ (f-h), and $\text{NiCo}_2\text{O}_4\text{EG}$ (j-i). Depth analysis, and FFT images constructed from selected regions are also presented.

2.67 nm, indicating that the shape changed without significantly altering the nanoparticle width. For the intermediate $\text{NiCo}_2\text{O}_4\text{EG}_{66}$ (Figures 2e–h), the SEM images at 25,000 \times magnification revealed agglomerated structures. However, higher-magnification HRTEM images at 100,000 \times and 800,000 \times show detailed needle-like nanorod structures. This suggests that the needle-like nanorods underwent structural modifications, leading to micrometer-scale agglomerations as the amount of reducing agent in the hydrothermal calcination synthesis increased.

The TEM images and depth profiles revealed significant differences in the structural properties of the synthesized materials, emphasizing the role of oxygen vacancies in modulating lattice characteristics. The TEM analysis of $\text{NiCo}_2\text{O}_4\text{DI}$ (Figures 2c and d) displayed a uniform crystalline structure with minimal dark regions, indicative of a low defect density. Depth profile measurements confirmed an interplanar distance of 4.82 Å, corresponding to the (111) plane of the cubic NiCo_2O_4

structure. This consistency in lattice spacing reflects high structural integrity with negligible distortions, establishing $\text{NiCo}_2\text{O}_4\text{DI}$ as the material with the most well-ordered lattice. In contrast, the TEM image of $\text{NiCo}_2\text{O}_4\text{EG}_{66}$ (Figures 2g) displayed a higher density of darker regions, signifying an increase in surface defects. Depth profile analysis (Figure 2h) showed a pronounced expansion of the interplanar distance to 5.6 Å, marking the largest deviation among all samples. This increase suggests significant lattice distortions and local stress relief caused by the presence of oxygen vacancies, making $\text{NiCo}_2\text{O}_4\text{EG}_{66}$ the material with the highest degree of lattice distortion. For $\text{NiCo}_2\text{O}_4\text{EG}$, depth profile analysis (Figures 2i) showed an interplanar distance of 5.15 Å, indicative of moderate stress relief and structural distortions attributable to oxygen vacancies.

Selected area electron diffraction (SAED) was performed to compare the XRD patterns of $\text{NiCo}_2\text{O}_4\text{DI}$ and $\text{NiCo}_2\text{O}_4\text{EG}$ (Figures S1a and S1b). The SAED patterns of $\text{NiCo}_2\text{O}_4\text{DI}$

exhibited more defined and brighter rings, which are characteristic of crystalline materials, with rings indexed to the Fd-3m (227) space group, a cubic spinel structure as previously described by XRD.^[18] This confirms the material's crystalline nature and the preservation of the spinel cubic structure. In contrast, the SAED pattern of NiCo₂O₄EG exhibited less defined rings, reflecting structural distortions caused by oxygen vacancies and increased defect density.

The progressive changes in morphology, defect density, and interplanar distances across the materials highlight the critical influence of synthesis parameters on structural properties.

The valence state analysis of the synthesized bimetallic oxides and the examination of surface defects were conducted using X-ray photoelectron spectroscopy (XPS). The high-resolution XPS spectra of the Ni_{2p}, Co_{2p} and O_{1s} core levels are depicted in Figure 3. The decomposition of the Ni_{2p} spectra was executed by simulating each contribution with two peaks corresponding to the Ni2p_{3/2} (855.4 eV) and Ni2p_{1/2} (872.6 eV) core levels, with a binding energy (BE) difference of 17.2 eV. The

Ni2p spectra of the spinel oxides displayed two prominent peaks, Ni²⁺ and Ni³⁺, for each core level. The distribution between these two valence states is a characteristic feature of spinel-type bimetallic oxides.^[19] As shown in Figure S2, there was an increase in the Ni³⁺/Ni²⁺ ratio with the growth of EG in the spinel synthesis. This phenomenon is attributed to the effect of the reducing agent on the spinel structure, favoring Ni³⁺ cations in the octahedral sites of the inverse spinel. According to literature, an increase in the Ni³⁺ electronic structure enhances the electrocatalytic performance for the oxygen evolution reaction (OER) owing to its optimal e_g orbital occupancy.^[20]

As depicted in Figures 3b, e, and h, the Co2p spectra reveal the presence of eight characteristic peaks: Co²⁺ (779.6 eV, 794.7 eV), Co³⁺ (781.5 eV, 796.6 eV), and four satellite peaks (784.2 eV, 788.0 eV, 800.0 eV and 804.6 eV).^[21] Unlike Ni, the Co²⁺/Co³⁺ ratio did not vary significantly across spinels synthesized with different EG percentages, as indicated in Figure S2, where catalytic activity dependence was observed

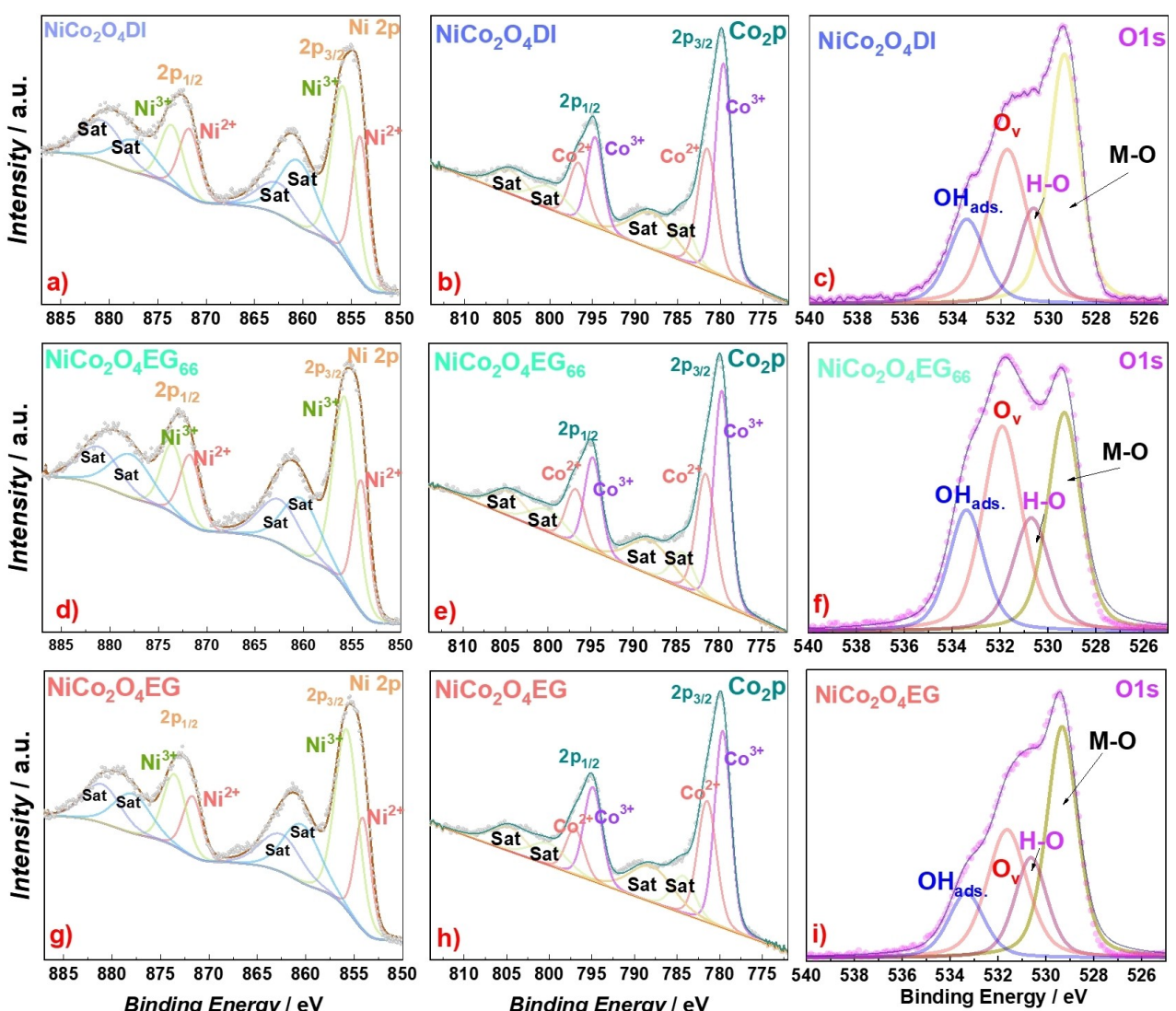


Figure 3. High-resolution XPS spectra of (a, d, and g) Ni 2p, (b, e, and h) Co 2p, and (c, f, and i) O 1s for NiCo₂O₄DI, NiCo₂O₄EG₆₆, and NiCo₂O₄EG, respectively

based on the proportion of Ni^{3+} in the material. The fitting parameters performed using the CasaXPS software for the Ni 2p and Co 2p spectra are provided in Tables S1 and S2.

The O1s spectra, as illustrated in Figures 4c, f, and i, were deconvoluted in accordance with established literature into three representative signals: metal-oxygen bonds (529.46 eV), surface defects such as oxygen vacancies (O_{vac}) (531.46 eV), and chemically adsorbed water (533.24 eV).^[21] The presence of oxygen vacancies is directly correlated with the EG content in the synthesis, with the relative area ratio shifting from 33.23% ($\text{NiCo}_2\text{O}_4\text{DI}$) to 38.07% ($\text{NiCo}_2\text{O}_4\text{EG}_{66}$). This increase in surface defects is expected to facilitate $\text{OH}^{<\text{M}->}$ and O_2 adsorption and diffusion, thereby boosting both the ORR and OER catalytic activities.^[20a,22]

Characterization of the carbonaceous support doped with nitrogen, and nitrogen-phosphorus heteroatoms was made by XPS as depicted in Figures 4a and b–c, respectively. For the deconvolution of the N1s signal peaks in N–C and P, N–C, four

principal nitrogen signals were presented in accordance with the literature.^[12,23] Pyridinic (398.3 eV), pyrrolic (400.8 eV), graphitic (402.6 eV), and oxidized (NO_x) (404.5 eV). Pyridinic nitrogen species, which are highly desirable for their strong affinity for OH^* adsorption, are present in N–C with a relative percentage of 34.5%. However, this percentage significantly decreased to 18.53% upon the addition of phosphorus in the doping process, likely because of the replacement of pyridinic nitrogen species by phosphorus heteroatoms in the carbon support network and the formation of P–N bonding. The binding energy signal associated with P2p (Figure 4c) was deconvoluted into three distinct signals: P–C (132.49 eV, 57.03%), P–N (133.51 eV, 24.97%), and P–O (134.47 eV, 18.00%).^[24] The P–C bond exhibited the largest relative area, indicating the presence of this heteroatom on the surface of the carbonaceous support. This is in contrast with the absence of this signal in the material doped solely with N, as observed in Figure S3. The uniform deposition of nickel cobaltite nanorods on the carbonaceous

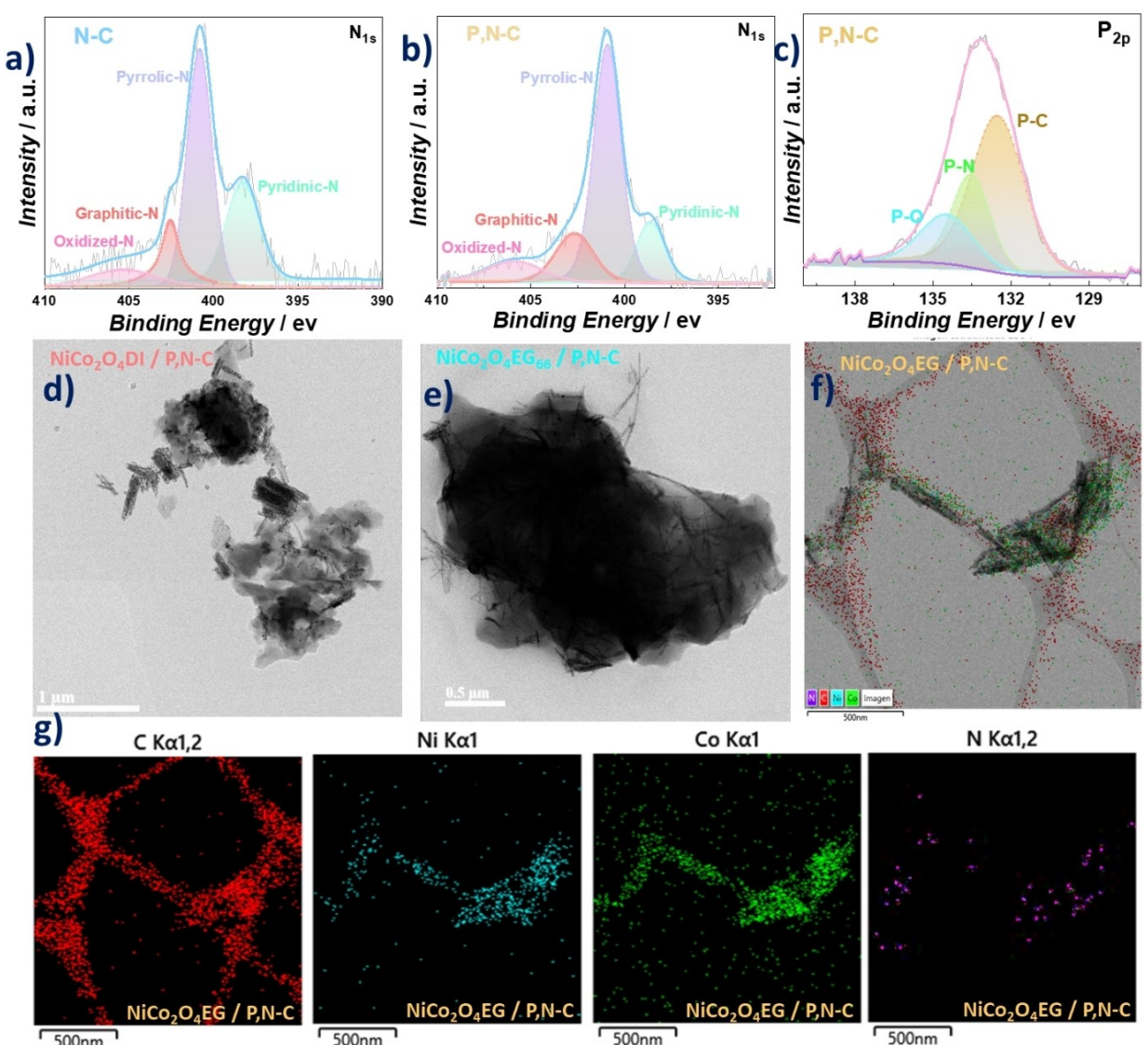


Figure 4. High-resolution XPS spectra of (a) N 1s for N–C, (b and c) N1s and P2p for P, N–C. (d, e and f) HR-TEM micrograph of $\text{NiCo}_2\text{O}_4\text{DI}/\text{P},\text{N}-\text{C}$, $\text{NiCo}_2\text{O}_4\text{EG}_{66}/\text{P},\text{N}-\text{C}$ and $\text{NiCo}_2\text{O}_4\text{EG}/\text{P},\text{N}-\text{C}$. (g) elemental maps for C, Ni, Co and N for $\text{NiCo}_2\text{O}_4\text{EG}/\text{P},\text{N}-\text{C}$.

support (P, N–C) was determined via high-resolution transmission electron microscopy (HR-TEM), as illustrated in Figures 4d, 4e, and 4f for the materials $\text{NiCo}_2\text{O}_4\text{DI}/\text{P,N-C}$, $\text{NiCo}_2\text{O}_4\text{EG}_{66}/\text{P,N-C}$, and $\text{NiCo}_2\text{O}_4\text{EG}/\text{P,N-C}$, respectively. In the latter case (Figure 4g), the elemental distributions of Ni and Co are uniform across the granular surface of the micrometrically agglomerated carbonaceous material, which contains low percentages of nitrogen.

Electrochemical Characterization

Regarding the oxygen evolution reaction (OER) performance of NiCo_2O_4 in relation to the carbonaceous support and the solvent used in the synthesis was investigated using linear scan voltammetry (LSV) in 1.0 M KOH at a scan rate of 5 mVs⁻¹, and compared with that of a precious metal compound, Pt/C: IrO₂/C ratio of 1:1 (Pt-IrO₂/C), as shown in Figure 5a.

For carbon support, $\text{NiCo}_2\text{O}_4\text{DI}/\text{N-C}$ and $\text{NiCo}_2\text{O}_4\text{DI}/\text{P,N-C}$ exhibit a marked difference in their electrocatalytic behavior. Introducing phosphorus into the carbonaceous material structure reduced the potential at 10 mAcm⁻² by approximately 120 mV. Additionally, a significant reduction in the Tafel slope was observed for the material doped with N and P, as presented in Figure S4b. This enhancement in the OER kinetics has been previously demonstrated in carbonaceous materials with P–N co-doping, which also shows reduced Tafel slopes.^[25] These

findings indicate that the incorporation of phosphorus into the composite enhances the reaction kinetics and leads to a notable increase in the number of active sites and conductivity. Moreover, the OER performance of materials synthesized with varying EG percentages and supported on P,N–C demonstrates an improvement in the overpotentials (η), with $\text{NiCo}_2\text{O}_4\text{EG}_{66}/\text{P,N-C}$ (297 mV) outperforming $\text{NiCo}_2\text{O}_4\text{DI}/\text{P,N-C}$ (310 mV) and $\text{NiCo}_2\text{O}_4\text{EG}/\text{P,N-C}$ (320 mV), as represented in Figure S4c. This potential difference is further illustrated in Figure 5a, with potential to 10 mAcm⁻² values of 1.52 V for $\text{NiCo}_2\text{O}_4\text{EG}_{66}/\text{P,N-C}$, compared to 1.54 V for $\text{NiCo}_2\text{O}_4\text{DI}/\text{P,N-C}$, and 1.55 V for $\text{NiCo}_2\text{O}_4\text{EG}/\text{P,N-C}$, following the reaction kinetics with Tafel slopes close to 105 mVdec⁻¹. $\text{NiCo}_2\text{O}_4\text{EG}_{66}/\text{P,N-C}$ demonstrated superior OER performance attributed to its higher oxygen vacancy content, moderately distorted lattice planes, and preserved nanorod structure. These features increase the availability of active sites and improve electrocatalytic stability, particularly for oxygen evolution.

This electrocatalytic behavior indicates promising performance for precious-metal-free materials. However, it still falls short of the performance exhibited by Pt-IrO₂/C, which has a Tafel slope of 74 mVdec⁻¹ and a potential of 1.42 V at 10 mAcm⁻², showing a potential difference of 96 mV compared with the best-synthesized catalyst, $\text{NiCo}_2\text{O}_4\text{EG}_{66}/\text{P,N-C}$.

The electrochemical profile of $\text{NiCo}_2\text{O}_4\text{EG}_{66}/\text{P,N-C}$ as representative material confirms activity for the oxygen reduction reaction (ORR, Figure S4a). The ORR evaluations were conducted in 0.1 M KOH using rotating-disk electrode voltammetry at rotation speeds ranging from 400 to 2400 rpm for the synthesized materials, as depicted in Figures 5b–e. The comparison of oxygen reduction properties as a function of the dopant in the carbonaceous support (Figures 5b and c) demonstrated superior performance for $\text{NiCo}_2\text{O}_4\text{DI}$ supported on P,N–C, with an onset potential (E_{onset}) of 0.95 V and a half-wave potential ($E_{1/2}$) of 0.84 V.

In contrast, supporting the material on N–C resulted in a decrease in E_{onset} by 0.14 V and $E_{1/2}$ by 0.17 V. The electron transfer numbers were calculated using the K–L equation,^[26] as shown in Figure S5a. $\text{NiCo}_2\text{O}_4\text{DI}/\text{N-C}$ (3.92e⁻), $\text{NiCo}_2\text{O}_4\text{EG}_{66}/\text{P,N-C}$ (3.92e⁻) and $\text{NiCo}_2\text{O}_4\text{DI}/\text{P,N-C}$ (3.4e⁻) exhibit kinetics predominantly following a 4e⁻ pathway involving the reduction of oxygen to OH⁻ species. In contrast, $\text{NiCo}_2\text{O}_4\text{EG}/\text{P,N-C}$ shows a tendency towards a 3.16 e⁻ transfer, indicating an intermediate pathway between the 4e⁻ and 2e⁻ processes.

To further validate these findings, RRDE measurements were performed to quantify the hydrogen peroxide (H₂O₂) yield, as depicted in Figure S5b. For $\text{NiCo}_2\text{O}_4\text{DI}/\text{N-C}$, the H₂O₂ yield was 19.7% at 0.3 V and 8.45% at 0.6 V, reflecting an incomplete reduction pathway compared to the ideal 4e⁻ mechanism. In contrast, $\text{NiCo}_2\text{O}_4\text{DI}/\text{P,N-C}$ exhibited a lower H₂O₂ yield of 6% at 0.3 V and 1.25% at 0.6 V, indicating a more efficient 4e⁻ pathway.

These results demonstrate that $\text{NiCo}_2\text{O}_4\text{DI}/\text{P,N-C}$ has superior catalytic activity for the ORR, as its lower H₂O₂ yield at both potentials aligns with the expected performance of high-efficiency ORR catalysts. For a catalyst to be considered highly effective in ORR applications, the H₂O₂ yield should remain

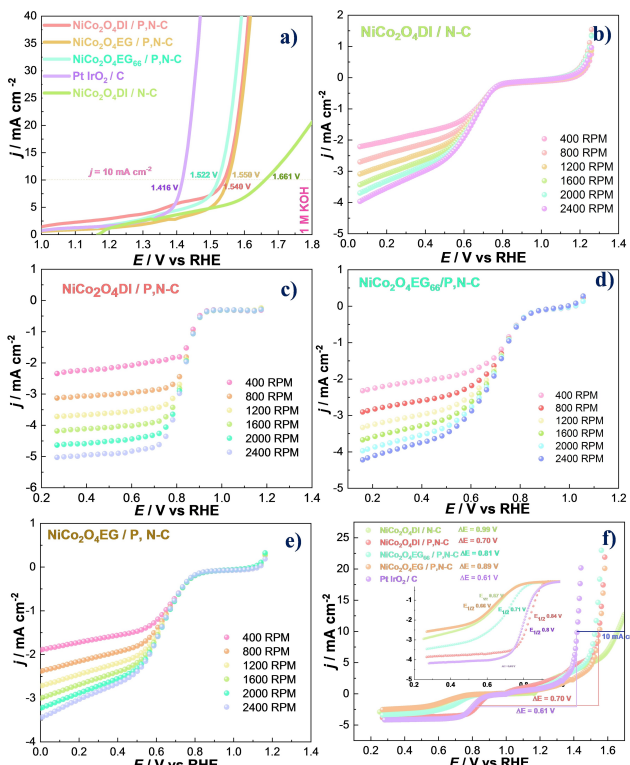


Figure 5. (a) OER activity at 1600 rpm for NiCo_2O_4 catalysts and Pt-IrO₂/C. (b–e) LSV at different rotation speeds of $\text{NiCo}_2\text{O}_4\text{DI}/\text{N-C}$, $\text{NiCo}_2\text{O}_4\text{DI}/\text{P,N-C}$, $\text{NiCo}_2\text{O}_4\text{EG}_{66}/\text{P,N-C}$, $\text{NiCo}_2\text{O}_4\text{EG}/\text{P,N-C}$, and Pt-IrO₂/C, respectively. (f) Bifunctionality plot of synthesized catalysts and Pt-IrO₂/C.

below 10%, particularly at relevant potentials, to minimize undesirable side reactions and maximize electron transfer to water.

These enhancements were attributed to the increased conductivity of the catalyst facilitated by the incorporation of phosphorus into the composite.^[27]

Additionally, the study of the effect of EG on the ORR electrocatalytic properties is evidenced in Figures 5b–e. The E_{onset} , $E_{1/2}$, and limiting current density (j_{lim}) decreased as higher EG percentages were used in the synthesis, as shown in Table S3. These values dropped from 0.95 V, 0.84 V, and -5 mA cm^{-2} for $\text{NiCo}_2\text{O}_4\text{DI}/\text{P,N-C}$ to 0.86 V, 0.66 V, and -3.5 mA cm^{-2} for $\text{NiCo}_2\text{O}_4\text{EG}/\text{P,N-C}$, respectively. This suggests that the electrocatalytic properties of nickel cobaltite for oxygen reduction decrease as the EG percentage increases, leading to structural modifications of the nanorods, as observed using microscopy techniques. In contrast, $\text{NiCo}_2\text{O}_4\text{DI}$ maintains constant interplanar distances, reflecting a more ordered structure and a less distorted crystalline lattice. This stability enhances efficient electron transfer between the metallic atoms (Ni and Co) and the P,N-doped carbon support, which is critical for oxygen reduction mechanisms. The less distorted structure also facilitates the formation of a homogeneous and efficient interface, characterized by a high density of well-defined active sites. These features promote the effective adsorption and reduction of oxygen species (O_2 , OH^-) during the ORR, ensuring superior catalytic performance.

Figure 5f and Table S3 summarize the relationship between the OER and ORR for the catalysts used along with their respective potential differentials (ΔE) between these reactions (E at 10 mA cm^{-2} – $E_{1/2}$). The lowest ΔE is observed for $\text{NiCo}_2\text{O}_4\text{DI}/\text{P,N-C}$ at 0.70 V, which significantly increases to 0.99 V in the absence of phosphorus as a dopant in the carbonaceous support. $\text{NiCo}_2\text{O}_4\text{EG}_{66}$ and $\text{NiCo}_2\text{O}_4\text{EG}$ exhibited higher ΔE values of around 0.81 and 0.89 V, respectively. This indicates a higher potential for using $\text{NiCo}_2\text{O}_4\text{DI}/\text{P,N-C}$ in Zn-air batteries, as they maintain a good balance between a nanorod microstructure with a high degree of surface defects and an adequately interfaced heteroatom-doped carbon support. When comparing this precious-metal-free material with the reference (Pt-IrO₂/C), the latter exhibits superiority, with a ΔE of 90 mV.

Application in Zinc-Air Battery

A custom-engineered zinc-air battery (ZAB) utilizing $\text{NiCo}_2\text{O}_4\text{DI}/\text{N-C}$, $\text{NiCo}_2\text{O}_4\text{DI}/\text{P,N-C}$, $\text{NiCo}_2\text{O}_4\text{EG}_{66}/\text{P,N-C}$, $\text{NiCo}_2\text{O}_4\text{EG}/\text{P,N-C}$, or Pt-IrO₂/C was developed to evaluate its practical application as an energy conversion and storage device. Electrochemical Impedance Spectroscopy (EIS) confirmed the proper assembly of these batteries, as depicted in Figure 6a, revealing similar internal resistance values, ranging between approximately 3.2–3.8 ohm cm².

The Nyquist plots exhibit a semicircular region at high frequencies and a diffusion-dominated region at low frequencies, typical of complete cell systems. These features correspond to the equivalent circuit model depicted in the inset of

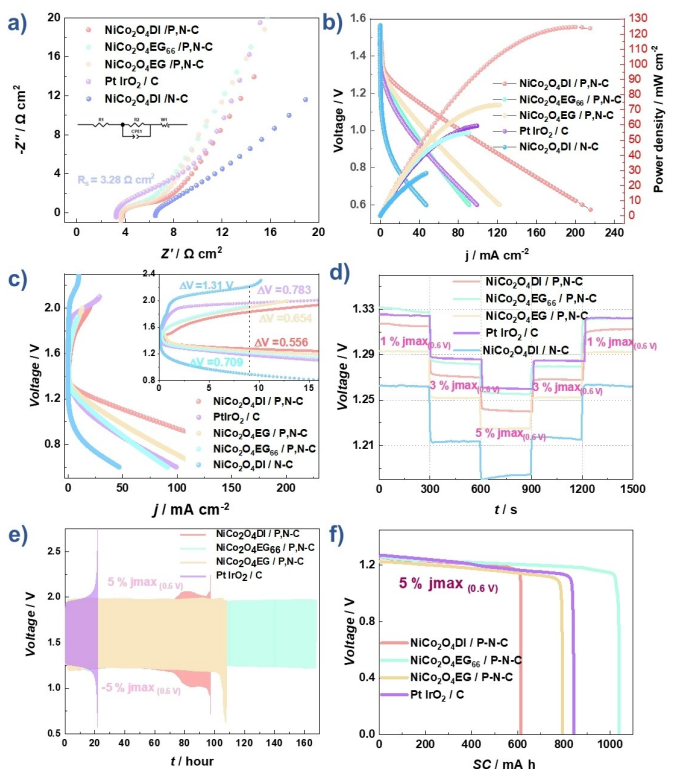


Figure 6. (a) Nyquist plots at OCV, (b) polarization and power density curves, (c) discharging and charging polarization curves, (d) discharging curves at different current densities, (e) charge/discharge cycles, and (f) specific capacity tests for NiCo_2O_4 synthesized catalysts and Pt-IrO₂/C.

Figure 6a and b were interpreted using simulations performed with ZView software. The extracted electrochemical parameters, summarized in Table S4, include the system's total resistance before polarization (R_1), the charge transfer resistance associated with redox kinetics (R_2), the double-layer capacitance represented by a constant phase element (CPE_1), and the Warburg impedance reflecting mass transport limitations (W_1).

As highlighted in Table S4, the electrochemical impedance spectroscopy (EIS) analysis identifies $\text{NiCo}_2\text{O}_4\text{DI}/\text{P,N-C}$ as the most efficient material, demonstrating the lowest charge transfer resistance ($R_2 = 265.7 \Omega$) and minimal diffusion impedance ($W_1 \cdot R = 3.90 \Omega$), which signify superior reaction kinetics and effective mass transport for Zn-air battery applications. In comparison, Pt-IrO₂/C exhibits competitive performance with a moderate charge transfer resistance ($R_2 = 312.4 \Omega$) and a high capacitance value ($CPE_1 \cdot T = 0.09 \text{ F s}^{-1}$), indicative of its capability to facilitate efficient charge transfer processes.

Conversely, $\text{NiCo}_2\text{O}_4\text{DI}/\text{N-C}$ shows the poorest performance, characterized by a significantly high charge transfer resistance ($R_2 = 2101.0 \Omega$) and diffusion impedance ($W_1 \cdot R = 107.6 \Omega$). These values underscore severe limitations in both charge transfer and mass diffusion processes, making it less suitable for high-performance Zn-air batteries under demanding energy conditions.

The discharge polarization behavior, illustrated in Figure 6b, highlighted the superior performance of $\text{NiCo}_2\text{O}_4\text{DI}/\text{P,N-C}$, which exhibited a notably higher peak power density

(124.4 mW cm⁻² at 215.8 mA cm⁻²) compared to the other cobaltite materials analyzed in Table S5, most of which displayed peak power densities below 100 mW cm⁻², including the reference Pt-IrO₂/C (58.9 mW cm⁻² at 99.3 mA cm⁻²). In contrast, NiCo₂O₄DI/N-C showed the poorest performance, with the lowest peak power density of 47.1 mW cm⁻², underscoring the importance of P doping in enhancing electrocatalytic activity.

The charge-discharge polarization curves, presented in Figure 6c, demonstrated the smallest voltage gap (ΔV) for NiCo₂O₄DI/P,N-C, approximately 0.55 V at a current density of 9 mA cm⁻², consistent with its superior performance in half-cell tests, indicating its potential as the most promising catalyst for rechargeable ZABs. Meanwhile, NiCo₂O₄DI/N-C exhibited a much larger and unfavorable voltage gap of 1.31 V under the same conditions, indicating significant limitations in its charge-discharge efficiency. These findings explicitly illustrate the beneficial effect of P doping in reducing the overpotential and improving energy efficiency.

Regarding energy delivery capability (Figure 6d), different percentages (1%, 3%, 5%, 3%, and 1%) of the maximum current density at 0.6 V (j_{\max} (0.6 V)) on the discharge curve were required based on the material evaluated. The nickel cobaltite catalysts exhibited superior voltage recovery compared to benchmark material.

The stability of the bifunctional materials was assessed through charge-discharge cycling using 5% j_{\max} (0.6 V) which are illustrated in Figure 6e. The ZAB with NiCo₂O₄DI/P,N-C achieved an initial charge voltage of 1.83 V and a discharge voltage of 1.36 V, with a ΔV of 0.48 V. This material exhibited the highest round-trip efficiency (RTE) of 74.3%, despite utilizing the highest current density of 10 mA cm⁻² among the evaluated

materials (Table S5), with no RTE values exceeding 60%, except for NiCo₂O₄@ reported by L. Wan et al.,^[28] which reached 65.7%. Pt-IrO₂/C and NiCo₂O₄EG₆₆/P,N-C showed the lowest RTE values of 68.2% and 67.5%, respectively. Over time, the benchmark material failed after 21 h of use. After 50 h, the RTE of NiCo₂O₄EG₆₆/P,N-C remained stable at 64.1%, closely followed by NiCo₂O₄DI/P,N-C, and NiCo₂O₄EG/P,N-C, with RTE values of 62.2% and 61.7%, respectively. NiCo₂O₄EG₆₆/P,N-C demonstrated the highest durability, exceeding 165 h of use, significantly outperforming other nickel cobaltite materials reported in the literature, which typically do not surpass 54 h under such high relative current densities of 5% j_{\max} (0.6 V), as shown in Table S5.

This behavior was corroborated in specific capacity tests, as shown in Figure 6f, where the 66% EG spinel displayed the highest specific capacity (SC) of 1039.6 mAh at a current density of 5 mA cm⁻². Pt-IrO₂/C showed an SC of 844.1 mAh at the same current density. Materials subjected to higher current densities exhibited lower SC values: 794.5 mAh (at 6 mA cm⁻²) and 616.5 mAh (at 10 mA cm⁻²). The results from performance steps, stability, and charge-discharge cycle tests underscored the exceptional long-term performance of materials with high surface defects and interfacial arrangements, such as NiCo₂O₄EG₆₆/P,N-C, with the highest SC and testing durations of up to 165 h.

Further stringent tests on NiCo₂O₄DI/P,N-C, which exhibited the highest potential in both half-cell tests and charge-discharge polarization curves, are depicted in Figures 7a-f. The superior stability of the material during charge/discharge cycles at various current densities (5, 10, 20, 30, and 40 mA cm⁻²) was also observed. Compared with the benchmark, the bifunctional material performed admirably up to 40 mA cm⁻², at which point

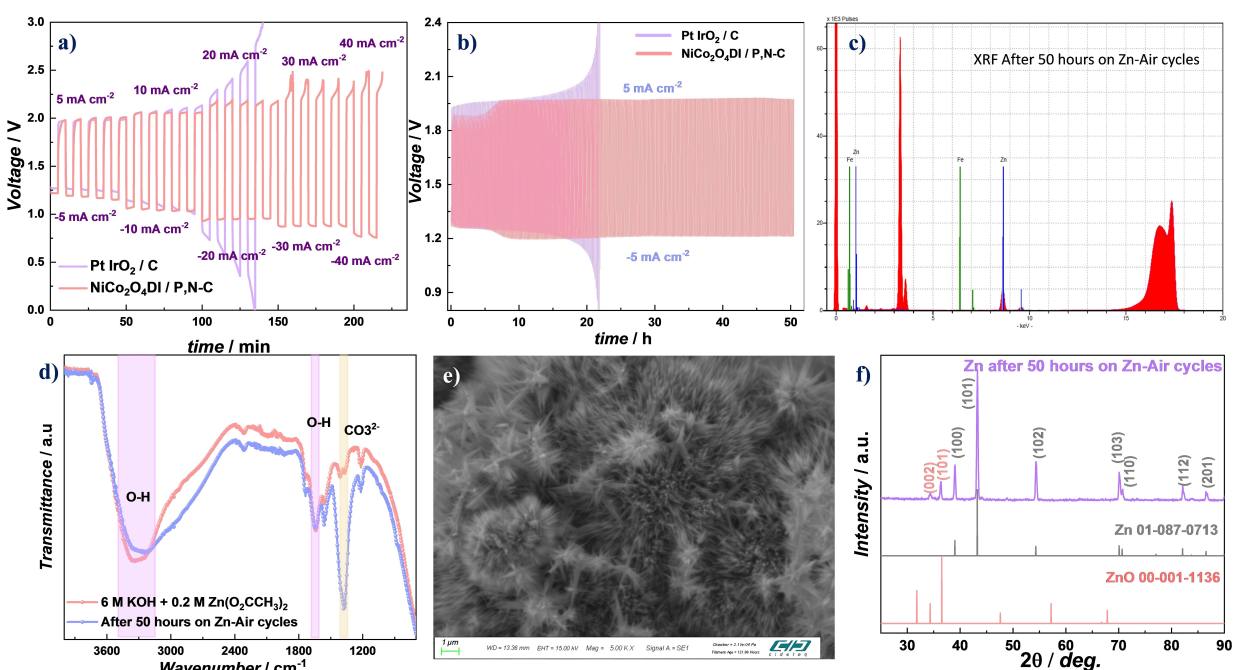


Figure 7. Charge/discharge cycle curves at (a) different current densities and (b) 5 mA cm⁻² for NiCo₂O₄DI/P,N-C, and Pt-IrO₂/C. Post-mortem characterization of NiCo₂O₄DI/P,N-C after 50 h of cycling performance (c and d) of the electrolyte by XRF and FTIR, and (e and f) of the Zn anode by SEM and XRD.

severe carbon corrosion processes began, generating carbonates and degrading the air electrode to the extent that it ruptured, causing electrolyte leakage. However, the discharge process-maintained voltages close to 0.78 V, indicating the catalyst's continued operational capability. In contrast, Pt-IrO₂/C began to fail at 20 mA cm⁻² in both the charge and discharge reactions, indicating active site saturation and a total loss of catalyst efficacy.

To further investigate the failure analysis of ZABs using the most promising bifunctional catalyst NiCo₂O₄DI/P,N-C, a charge-discharge cycling test was conducted over 50 h at a current density of 5 mA cm⁻² with a cycle duration of 15 min, as shown in Figure 7b. Upon completion, the electrolyte and Zn anode were physiochemically characterized. The electrolyte (6 M + 0.2 M Zn(O₂CCH₃)₂) was analyzed via XRF (Figure 7c), revealing the presence of K and Zn from the electrolyte and anode oxidation, and Fe as a reference material used in the technique. This confirms the absence of transition metals (Ni and Co) from the catalyst, confirming the excellent stability of Ni cobaltite. FTIR analysis (Figure 7d) of the electrolyte after 50 h of use (blue graph) compared to the unused electrolyte (red graph) highlighted a significant signal at 1381 cm⁻¹ corresponding to carbonates (CO₃²⁻), indicative of carbon corrosion during ZAB charge reactions at the air electrode at voltages near 1.9 V over prolonged periods. This carbon was present in both the SIGRACET collector and the P,N-C carbon support.

The Zn anodes used during the 50 h cycles were characterized by SEM and XRD (Figures 7e, S6, and 7f). SEM images at 5 K magnification showed Zn electrodeposits during ZAB charge reactions, with dendritic growth of metal oxide in cluster-like spines. XRD analysis of the anode compared to crystallographic cards (01-087-0713 and 00-001-1136) confirmed that the observed peaks matched the planes of metallic Zn predominantly, with superficial ZnO, confirming that the needle-like structures in the SEM micrographs were ZnO formations. The most intense peak for ZnO, the (101) plane, corresponds to the growth of ZnO nanoparticles.^[29]

Physicochemical characterization of the electrolyte and Zn anode after 50 h of cycling confirmed the stability of the Ni cobaltite catalyst and identified carbon corrosion as a primary degradation mechanism. Growth of ZnO nanoparticles on the anode surface was observed, corresponding to the (101) plane. These findings underscore the potential of NiCo₂O₄DI/P, N-C as promising catalysts for rechargeable ZABs, warranting further investigation to optimize their performance and commercial viability.

To elucidate the observed conductivity, it is important to analyze the changes in the electronic structure of the support. Figure 8 illustrates the projected density of states (PDOS) for carbon systems doped with nitrogen (N) and phosphorus (P). The vertical axis represents energy relative to the Fermi level, while the horizontal axis shows the normalized PDOS. Each panel highlights contributions from carbon atoms (black line) and dopants (blue for N, red for P). In all cases, we can observe the metallic character of the system. However, different configurations lead to varying densities of states at the Fermi

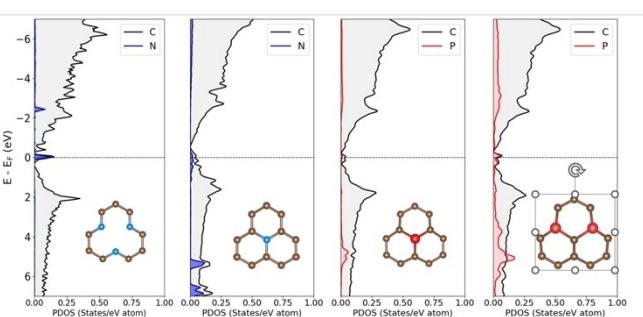


Figure 8. PDOS for N and P doped carbons in different configurations.

level, which is expected to have a marked influence on the system's conductivity. Notably, nitrogen atoms in the pyridinic configuration and phosphorus in the substitutional configuration exhibit a significant contribution of density of states around the Fermi level. In this way, we can establish that the combination of N and P tends to increase the number of states at the Fermi level and charge transfer, with a synergistic effect. These electronic differences in the support explain variations in material conductivity. Such insights illuminate the underlying mechanisms that drive the measured electrical conductivity in this system.

Conclusions

Interface engineering achieved through the integration of two materials with high surface defect density, namely nickel cobaltite with oxygen vacancies and phosphorus and nitrogen-doped carbon supports, significantly enhanced the oxygen evolution reaction (OER) and oxygen reduction reaction (ORR). Electrochemical measurements revealed substantial reductions in the overpotential and Tafel slope of the NiCo₂O₄DI/P, N-C composites, which can be attributed to the improved conductivity and increased active site density resulting from N-P co-doping. Computational studies employing DFT + U calculations offered insights into the electronic structure modifications and interaction energies at the catalyst interfaces, corroborating the observed experimental trends. Proof-of-concept testing of ZABs revealed the highest round-trip efficiency of 74.3%, long-term cycle stability of up to 100 h, and strong performance during charging/discharging cycles with current densities exceeding 30 mA cm⁻². These results clearly establish their potential as practical catalysts in high-efficiency and long-life ZABs for developing durable and efficient energy-storage solutions.

Experimental Section

Nickel cobaltite (NiCo₂O₄) nanoparticles were synthesized using a solvothermal method with defect-promoting ethylene glycol, followed by calcination at 350 °C. These were paired with nitrogen- and phosphorus-doped carbon composites (N-C and P, N-C) derived from polyaniline (PANI) to enhance the interface for

improved battery rechargeability. Electrochemical tests were performed with rotating disk electrodes to evaluate oxygen reduction and evolution reactions, key to Zn-air battery performance. A Zn-air battery prototype, assembled with catalyst-coated air electrodes and zinc anodes, was tested in a KOH-based electrolyte. Charge and discharge cycles were conducted to measure polarization, power density, and specific capacity at various current densities. Post-test characterization of the electrolyte and zinc deposits, through XRF, FTIR, and SEM, provided insights into material stability and efficiency under high energy demand, and the full description is presented in the Supporting information.

Acknowledgements

The authors acknowledge the financial support provided by the Mexican council of humanities, science and technology (CONAHCYT) through the program Science Frontiers project grant 39569. The authors also acknowledge the technical support provided by Raul Ochoa and Anabel De la Cruz Delgado from CIMA V for the acquisition of TEM and SEM images. Similarly, we acknowledge the technical support of Susana Gaucin Gutiérrez from CIDETEQ for XRD and post-mortem SEM images.

Conflict of Interests

The authors declare no conflict of interest.

Data Availability Statement

The data that support the findings of this study are available from the corresponding author upon reasonable request.

Keywords: Zn-air battery • Nickel cobaltite • Bifunctional electrocatalyst • Interface engineering • Nitrogen doped carbon.

- [1] K. M. Tan, T. S. Babu, V. K. Ramachandaramurthy, P. Kasinathan, S. G. Solanki, S. K. Raveendran, *J. Energy Inst.* **2021**, *39*, 102591.
- [2] a) K. Zahra, T. Noor, N. Iqbal, N. S. Akbar, *J. Energy Inst.* **2024**, *88*, 111565; b) J. Fu, R. Liang, G. Liu, A. Yu, Z. Bai, L. Yang, Chen, *Adv. Mater.*, Wiley-VCH Verlag, **2019**, 1805230.
- [3] a) G. Zubi, R. Dufo-López, M. Carvalho, G. Pasaooglu, *Renewable Sustainable Energy Rev.* **2018**, *89*, 292–308; b) M. Patel, K. Mishra, R. Banerjee, J. Chaudhari, D. K. Kanchan, D. Kumar, *J. Energy Chem.* **2023**, *81*, 221–259.
- [4] H. Li, X. Cao, Y. Liu, Y. Shao, Z. Nan, L. Teng, W. Peng, J. Bian, *Energy Rep.* **2022**, *8*, 6258–6269.
- [5] M. Asmare, M. Zegeye, A. Ketema, *Energy Reports*. Elsevier Ltd June **2024**, *11*, 1199–1211.
- [6] a) Y. Han, C. Zhou, B. Wang, Y. Li, L. Zhang, W. Zhang, Y. Huang, R. Zhang, *Chem Catalysis* **2022**, *2*, 3357–3394; b) J. Fu, Z. P. Cano, M. G. Park, A. Yu, M. Fowler, Z. Chen, *Adv. Mater.* **2017**, *29*, 1604685.
- [7] L. L. Zhao, S. Zhao, N. Zhang, P. F. Wang, Z. L. Liu, Y. Xie, J. Shu, T. F. Yi, *Energy Storage Mater.* **2024**, *71*, 103628.
- [8] D. Yang, J. Li, C. Liu, W. Xing, J. Zhu, *J. Energy Chem.* **2023**, *82*, 122–138.
- [9] a) M. Etesami, R. Khezri, S. R. Motlagh, M. Gopalakrishnan, P. Mano, S. Namuangruk, S. Wannapaiboon, T. Yonezawa, A. Somwangthanaroj, S. Kheawhom, *Mater. Today Energy* **2024**, *44*, 101649; b) S. Ren, X. Duan, S. Liang, M. Zhang, H. Zheng, *J. Mater. Chem. A: Royal Society of Chemistry* **2020**, *8*, 6144–6182.
- [10] a) J. Liu, Z. Luo, J. Wu, D. Qian, W. Liao, G. I. N. Waterhouse, X. Chen, *Inorg. Chem.* **2024**, *63*(27), 12681–12689; b) G. Dias, S. Costa, J. M. Almeida, A. F. de Neto, *Adv. Colloid Interface Sci.* **2023**, *315*, 102891.
- [11] a) L. Fu, Y. Yao, J. Ma, Z. Zhang, G. Wang, W. Wei, *Langmuir* **2024**, *40*(13), 6990–7000; b) L. Fu, J. Ma, Z. Zhang, G. Wang, Y. Yao, W. Wei, *Vacuum* **2024**, *224*, 113163.
- [12] J. Béjar, F. Espinosa-Magaña, J. Avelar, A. Aguilar-Elguezabal, M. Guerra-Balcázar, N. Arjona, L. Álvarez-Contreras, *Carbon* **2023**, *204*, 411–426.
- [13] a) Y. Tao, W. Jiang, H. Wang, W. Hao, Q. Bi, X. Liu, J. Fan, G. Li, *J. Colloid Interface Sci.* **2024**, *657*, 921–930; b) W. Zhang, B. Feng, L. Huang, Y. Liang, J. Chen, X. Li, Z. Shi, N. Wang, *Appl. Catal. B Environ. Energy* **2024**, *358*, 124450; c) X. Lin, L. Cui, X. Ding, Y. Chen, Q. Wei, Z. Huang, B. Xie, *J. Alloys Compd.* **2024**, *998*, 174805.
- [14] a) R. Su, X. Tao, K. Zheng, L. Jiao, C. Zhang, R. Yang, H. Xie, X. Meng, C. Xu, *Carbon* **2024**, *225*; b) Z. Yuan, M. Fan, Y. D. Wang, Y. Cheng, H. Zhang, *ACS Appl. Energ. Mater.* **2024**, *7*(4), 1598–1605.
- [15] Y. Zhai, H. Mao, P. Liu, X. Ren, L. Xu, Y. Qian, *J. Mater. Chem. A* **2015**, *3*(31), 16142–16149.
- [16] a) D. Cai, Q. Cao, J. Du, Y. Liu, F. Bu, Y. Yan, X. Lu, Q. Xia, D. Zhou, Y. Xia, *Batteries & Supercaps* **2022**, *5*(3); b) Y. Ma, W. Shang, W. Yu, X. Chen, W. Xia, C. Wang, P. Tan, *Energy Fuels* **2021**, *35*(17), 14188–14196.
- [17] A. K. Das, S. Jena, S. Sahoo, R. Kuchi, D. Kim, T. A. Aljohani, G. C. Nayak, J. R. Jeong, *J. Saudi Chem. Soc.* **2020**, *24*(5), 434–444.
- [18] J. Wang, Z. Wu, L. Han, R. Lin, H. L. Xin, D. Wang, *ChemCatChem* **2016**, *8*(4), 736–742.
- [19] a) P. Kumaravel, S. K. Krishna, D. Navaneethan, R. Ramesh, *Electrochim. Acta* **2024**, *499*, 144656; b) Y. Tao, W. Jiang, H. Wang, W. Hao, Q. Bi, X. Liu, J. Fan, G. Li, *J. Colloid Interface Sci.* **2024**, *657*, 921–930.
- [20] a) O. Ambriz-Peláez, J. Béjar, A. D. Delgado, C. Rodríguez-González, C. M. Ramos-Castillo, L. Álvarez-Contreras, M. Guerra-Balcázar, N. Arjona, *FlatChem* **2024**, *45*, 100664; b) Y. Liu, P. Liu, W. Qin, X. Wu, G. Yang, *Electrochim. Acta* **2019**, *297*, 623–632.
- [21] a) W. Liu, J. Bao, L. Xu, M. Guan, Z. Wang, J. Qiu, Y. Huang, J. Xia, Y. Lei, H. Li, *Appl. Surf. Sci.* **2019**, *478*, 552–559; b) M. Kim, J. H. Hong, K. B. Kim, H. Y. Koo, Y. C. Kang, *Int. J. Energy Res.* **2024**, *2024*, 4459617; c) B. Ma, C. Zhang, Y. Zhou, *Int. J. Hydrogen Energy* **2024**, *56*, 552–561.
- [22] D. Lim, H. Kong, C. Lim, N. Kim, S. E. Shim, S. H. Baeck, *Int. J. Hydrogen Energy* **2019**, *44*(42), 23775–23783.
- [23] L. S. Bezerra, M. Mooste, G. V. Fortunato, S. F. Cardoso, R. V. Lanza, M. Tammeveski, K. Maia, *J. Electroanal. Chem.* **2023**, *928*, 117000.
- [24] a) Z. Li, S. Ji, H. Liu, C. Xu, C. Guo, X. Lu, H. Sun, S. Dou, S. Xin, J. H. Horton, C. He, *Adv. Funct. Mater.* **2024**, *34*(18), 2314444; b) S. Wu, H. Peng, J. Xu, L. Huang, Y. Liu, X. Xu, Y. Wu, Z. Sun, *Carbon* **2024**, *218*, 118756.
- [25] S. Chen, L. Zhao, J. Ma, Y. Wang, L. Dai, J. Zhang, *Nano Energy* **2019**, *60*, 536–544.
- [26] H. Li, S. Askari, J. Wang, N. Wolff, M. Behrens, L. Kienle, J. Benedikt, *Int. J. Hydrogen Energy* **2023**, *48*(67), 26107–26118.
- [27] a) A. Chen, Q. Yi, K. Sheng, Y. Wang, J. Chen, K. Xiang, H. Nie, X. Zhou, *Sustain. Energy Fuels* **2021**, *5*(9), 2458–2468; b) W. Li, Y. Li, H. Fu, G. Yang, Q. Zhang, S. Chen, F. Peng, *Chem. Eng. J.* **2020**, *381*, 122683.
- [28] L. Wan, Z. Zhao, X. Chen, P. F. Liu, P. Wang, Z. Xu, Y. Lin, B. Wang, *ACS Sustainable Chem. Eng.* **2020**, *8*(30), 11079–11087.
- [29] a) V. L. Patil, S. A. Vanalakar, A. S. Kamble, S. S. Shendage, J. H. Kim, P. S. Patil, *RSC Adv.* **2016**, *6*(93), 90916–90922; b) S. A. Vanalakar, S. S. Mali, R. C. Pawar, D. S. Dalavi, A. V. Mohalkar, H. P. Deshamukh, P. S. Patil, *Ceram. Int.* **2012**, *38*(8), 6461–6467.
- [30] a) G. Kresse, J. Hafner, *Phys. Rev. B* **1993**, *47*(1), 558–561; b) G. Kresse, J. Furthmüller, *Comput. Mater. Sci.* **1996**, *6*(1), 15–50; c) G. Kresse, J. Furthmüller, *Phys. Rev. B: Condens. Matter Mater. Phys.* **1996**, *16*(54), 11169–11186; d) G. Kresse, D. Joubert, *Phys. Rev. B* **1999**, *59*(3), 1758–1775.
- [31] S. Dudarev, G. Botton, *Phys. Rev. B: Condens. Matter Mater. Phys.* **1998**, *57*(3), 1505–1509.
- [32] X. Shi, S. L. Bernasek, A. Selloni, *J. Phys. Chem. C* **2016**, *120*(27), 14892–14898.
- [33] M. Methfessel, A. T. Paxton, *Phys. Rev. B* **1989**, *40*(6), 3616–3621.
- [34] H. J. Monkhorst, J. D. Pack, *Phys. Rev. B* **1976**, *13*(12), 5188.
- [35] S. Grimme, J. Antony, S. Ehrlich, H. Krieg, *J. Chem. Phys.* **2010**, *132*(15), 154104.
- [36] a) W. Liu, J. Bao, L. Xu, M. Guan, Z. Wang, J. Qiu, Y. Huang, J. Xia, Y. Lei, H. Li, *Appl. Surf. Sci.* **2019**, *478*, 552–559; b) H. Li, J. Wang, T. Tjardts, I. Barg, H. Qiu, M. Müller, J. Krahmer, S. Askari, S. Veziroglu, C. Aktas, L. Kienle, J. Benedikt, *Small* **2024**, *20*(24), 2310660; c) P. Tan, Z. Wu, B.

Chen, H. Xu, W. Cai, S. Jin, Z. Shao, M. Ni, *J. Electrochem. Soc.* **2019**, 166(14), A3448–A3455; d) C. Alegre, C. Busacca, A. Di Blasi, C. Cannilla, O. Barbera, V. Antonucci, M. J. Lázaro, V. Baglio, *J. Energy Storage* **2022**, 55, 105404; e) J. Yin, Y. Li, F. Lv, Q. Fan, Y. Q. Zhao, Q. Zhang, W. Wang, F. Cheng, P. Xi, S. Guo, *ACS Nano* **2017**, 11(2), 2275–2283; f) J. Béjar, L. Álvarez-Contreras, F. Espinosa-Magaña, J. Ledesma-García, N. Arjona, L. G. Arriaga, *Electrochim. Acta* **2021**, 391, 138900.
[37] a) Y. Li, Z. Zhou, G. Cheng, S. Han, J. Zhou, J. Yuan, M. Sun, L. Yu, *Electrochim. Acta* **2020**, 341, 135997; b) J. Qian, X. Bai, S. Xi, W. Xiao,

D. Gao, J. Wang, *ACS Appl. Mater. Interfaces* **2019**, 11(34), 30865–30871.

Manuscript received: November 4, 2024
Revised manuscript received: January 6, 2025
Accepted manuscript online: January 16, 2025
Version of record online: January 31, 2025
